Numerical Approximation to the General Kinetic Model for ASL Quantification

Nam G. Lee[1], Ahsan Javed[2], Terrence R. Jao[1], Krishna S. Nayak[2]

[1] Department of Biomedical Engineering, University of Southern California, Los Angeles, California, USA

[2] Ming Hsieh Department of Electrical and Computer Engineering, University of Southern California, Los Angeles, California, USA

Correspondence to:

Nam G. Lee, MS

3740 McClintock Ave, EEB 414

University of Southern California

Los Angeles, CA, 90089-2564

Phone: (213) 471-5668

E-mail: namgyunl@usc.edu

Journal:	Magnetic Resonance in Medicine (Note)
Running Title:	Numerical Approximation to the GKM for ASL Quantification
Word Count:	3485 (max 2800 words)
Figure Count:	7 figures (5 figures + 2 supporting figures)
Table Count:	1 table
Grant Support:	NIH/NHLBI R01-HL130494;

A preliminary version of this work was presented at ISMRM 2019 (Abstract #2191).

Abstract

Purpose: To develop a numerical approximation to the general kinetic model (**GKM**) for ASL quantification that will enable greater flexibility in ASL acquisition methods.

Theory: The Bloch-McConnell equations are extended to include the effects of single compartment inflow and outflow on both the transverse and longitudinal magnetization. These can be solved using an extension of Jaynes' matrix formalism with piecewise constant approximation of incoming labeled arterial flow and a clearance operator for outgoing venous flow.

Methods: The proposed numerical approximation is compared with GKM using simulations of pulsed labeling (**PASL**) and pseudo-continuous labeling (**PCASL**) and a broad range of transit time and bolus duration for tissue blood flow of 0.6 mL/g/min. Accuracy of the approximation is studied as a function of the timestep using Monte-Carlo simulations. Three additional scenarios are demonstrated: 1) steady-pulsed ASL (**spASL**); 2) MR fingerprinting ASL (**MRF-ASL**); 3) balanced steady-state free precession (**bSSFP**) and spoiled gradient-echo (**SPGR**) sequences.

Results: The proposed approximation was found to be arbitrarily accurate for PASL and PCASL labeling. PASL(PCASL) approximation error compared to GKM was <0.002%(<0.002%) and <0.05%(<0.05%) for timesteps of 3 and 35 msec, respectively. The proposed approximation matched well with customized signal expressions of spASL and MRF-ASL. The simulations of simultaneous modeling of flow, T_2, and MT showed an increase in steady-state bSSFP and SPGR signals.

Conclusion: We demonstrate a numerical approximation of the BMF equations that enables arbitrarily accurate modeling of PASL and PCASL signals comparable to GKM. This enables increased flexibility in the experiment design for quantitative ASL.

Keywords: Arterial Spin Labeling, Perfusion, Blood Flow, Quantification, Steady-Pulsed ASL, Fingerprinting ASL

1. INTRODUCTION

Tissue perfusion is an important indicator of organ health that can be measured by MRI with or without contrast agents. ASL is the most widely used non-contrast approach, and has been extensively applied to brain (1), kidney (2), and more recently heart (3). ASL involves labeling upstream blood using radiofrequency (**RF**) pulses and then imaging tissue as it is perfused, within the relatively short window of T1 relaxation.

ASL quantification was first demonstrated using Detre's "apparent-T1" approach (4,5) that combines the longitudinal component of the Bloch equations with single-compartment kinetics and derives an analytical expression for the longitudinal magnetization in the presence of flow. Buxton's general kinetic model (**GKM**) (6) reformulates Detre's "apparent-T1" approach as a convolution problem without requiring the Bloch equations, under a general setting where the transit delay and bolus duration are taken into account. GKM is widely used because it is simple, analytic, and provides excellent intuition into signal formation. However, it is nontrivial for GKM to model the effects of flow with magnetization transfer (**MT**) (7–9), T_2 effects, off-resonance, and irregular timing of labeling.

Many previous approaches in ASL have generalized the Bloch equations to include transit delay and bolus duration (10), MT effects (11–15), water exchange (16–18), and dispersion (19–21). However, all approaches tried to generalize only the longitudinal component of the Bloch equations and thus simultaneous modeling of flow with T_2 effects and off-resonance has not been demonstrated.

Unlike the approaches in ASL, the full Bloch equations (containing both transverse and longitudinal magnetization) have been extended with additional terms to model the physical phenomenon of interest. Examples include the Bloch-Torrey equations for diffusion (22) and velocity (23), and the Bloch-McConnell equations for magnetization transfer (24) and chemical exchange saturation transfer (25,26). These modified Bloch equations are efficiently solved with a variant of propagator approaches (i.e., matrix formalism) (27,28). Inspired by its great flexibility to model various effects, this work seeks to develop a framework based on matrix formalism that can simultaneously model the effects of flow with the aforementioned effects. We extend the Bloch equations with MT effects (a binary spin-bath model) (29–31) by adding single compartment inflow and outflow terms. We denote these "Bloch-McConnell-Flow" (**BMF**) equations.

In order to solve the BMF equations, we derive an extension of Jaynes' matrix formalism (32) with two approximations. This approach retains the advantages of Jaynes' matrix formalism, such as the ability to include off-resonance, the slice excitation profile, and B1 transmit (**B1+**) inhomogeneity. This numerical approach is particularly attractive for ASL scenarios that have been cumbersome for existing

GKM-based approaches, such as irregular timing of labeling (33,34), transient-state signal evolutions such as balanced steady-state free precession (**bSSFP**) steady-pulsed ASL (**spASL**) (35) and MR fingerprinting ASL (**MRF-ASL**) (36,37).

We first present the proposed BMF equations, and then the extended matrix formalism with numerical approximation. We demonstrate that accuracy depends on the timestep used for updating magnetization states. The numeric approximation is validated against GKM for the case of single-compartment kinetics with pulsed labeling and pseudo-continuous labeling. Monte-Carlo simulations are then used to investigate the impact of the timestep on the accuracy of a numeric approximation compared to GKM. The flexibility of this approach is demonstrated using two non-standard ASL pulse sequences. For each sequence our approach was validated against the existing quantification models.

2. THEORY

2.1 Bloch-Flow Equations

For simplicity, we assume single-compartment kinetics, instantaneous mixing between arterial blood water and tissue, and only the longitudinal magnetization of inflowing arterial blood is modified. For tissue magnetization $\mathbf{M}(t) = [M_x(t), M_y(t), M_z(t)]^T$ under perfusion, the proposed Bloch-Flow equations (in the rotating frame) model the effects of incoming arterial flow (constant unlabeled and time-varying labeled longitudinal magnetization) and outgoing venous flow on the transverse and longitudinal magnetization

$$\frac{d\mathbf{M}(t)}{dt} = \mathbf{M}(t) \times \gamma\mathbf{B}(t) - \frac{M_x(t)\vec{i} + M_y(t)\vec{j}}{T_2} + \frac{(M_0 - M_z(t))\vec{k}}{T_1} + \left(\frac{F}{\lambda}M_0 + s(t)\right)\vec{k} - \frac{F}{\lambda}(M_x(t)\vec{i} + M_y(t)\vec{j} + M_z(t)\vec{k}), \quad [1]$$

where M_0 is the equilibrium magnetization/g of tissue, F is the perfusion in mL of blood/g of tissue/min, λ is the tissue-blood partition coefficient in mL of blood/g of tissue, and $s(t)$ is referred to as the ASL bolus signal. Note that the model implicitly assumes ${M_0}^{\text{blood}} = {M_0}^{\text{tissue}}/\lambda$. Equation 1 can be expressed in matrix-vector notation, as follows:

$$\begin{bmatrix} \frac{dM_x}{dt} \\ \frac{dM_y}{dt} \\ \frac{dM_z}{dt} \end{bmatrix} = \begin{bmatrix} -\left(\frac{1}{T_2}+\frac{F}{\lambda}\right) & \gamma\mathbf{G}(t)\cdot\mathbf{r}+2\pi\Delta f & -\gamma B_{1,y}(t) \\ -(\gamma\mathbf{G}(t)\cdot\mathbf{r}+2\pi\Delta f) & -\left(\frac{1}{T_2}+\frac{F}{\lambda}\right) & \gamma B_{1,x}(t) \\ \gamma B_{1,y}(t) & -\gamma B_{1,x}(t) & -\left(\frac{1}{T_1}+\frac{F}{\lambda}\right) \end{bmatrix} \begin{bmatrix} M_x \\ M_y \\ M_z \end{bmatrix} + \begin{bmatrix} 0 \\ 0 \\ \left(\frac{1}{T_1}+\frac{F}{\lambda}\right)M_0 + s(t) \end{bmatrix}, \quad [2]$$

where $\mathbf{G}(t)\cdot\mathbf{r}$ is the dot product of a gradient vector $\mathbf{G}(t)$ in G/cm and a spatial position vector $\mathbf{r}$ in cm, Δf is off-resonance in Hz, $B_{1,x}(t)$ and $B_{1,y}(t)$ are the x and y components of an RF pulse in G. Note that the ASL bolus signal is the magnetization flow rate per g of tissue, expressed in units of magnetization/g of tissue/sec. The Bloch-Flow equations possess three additional features compared with the original Bloch equations: 1) the clearance of transverse and longitudinal magnetization by venous flow is present in the main diagonal and forms apparent T_2 and T_1 relaxation times for transverse and longitudinal magnetization, respectively, 2) unlabeled arterial blood is constantly added to the longitudinal magnetization creating a blood flow dependent equilibrium magnetization, and 3) time-varying labeled arterial blood decreases the longitudinal magnetization and creates a time-dependent equilibrium magnetization (Note $s(t)$ has the negative sign).

The theory is applicable for different labeling patterns and methods. We assume a perfectly rectangular bolus of arterial blood for PASL. The ASL bolus signal is defined differently for PASL and continuous ASL (**CASL**)/pseudo-continuous ASL (**PCASL**):

PASL: $$s(t) = \sum_{i=1}^{M} -\frac{F}{\lambda} M_0 \alpha_0 e^{-(t-t_{\ell,i})/T_{1b}} \left(u\left(t - t_{\ell,i} - T_{D,i}\right) - u\left(t - t_{\ell,i} - T_{D,i} - T_{W,i}\right)\right), \quad [3a]$$

CASL/ (PCASL): $$s(t) = -\frac{F}{\lambda} M_0 \alpha_0 e^{-T_D/T_{1b}} \left(u(t - T_D) - u(t - T_D - T_W)\right), \quad [3b]$$

where M is the number of labeling pulses, $t_{\ell,i}$ is the application of the i^{th} labeling, α_0 is the labeling efficiency (1 for saturation, 2 for inversion, 0 for control), T_{1b} is the longitudinal relaxation time of arterial blood, $\mathrm{u}(t)$ is the Heaviside step function, T_D is the arterial transit time (ATT) in sec, and T_W is the bolus duration in sec. In general, the ASL bolus signal $s(t)$ can be obtained from either an analytical expression or a numerical computation (e.g., dispersion (19,21)) as long as it can be evaluated at a particular time t.

2.2 Bloch-McConnell-Flow equations

The Bloch-Flow equations can be further extended to include MT effects. The binary spin-bath MT model (30,31) divides tissue magnetization between a liquid pool (f) of free water and a semisolid pool (s) of protons bound to macromolecules and neglects net exchange of transverse magnetization due to a very short transverse relaxation time of the semisolid pool $T_2^s \approx 10\mu s$ (38). Following previous approaches (11,13,39), we assume that blood water spins exchange only with the liquid pool of tissue magnetization. For free water and semisolid pool protons $\mathbf{M}(t) = [M_x^f(t), M_y^f(t), M_z^f(t), M_z^s(t)]^T$ under perfusion, the BMF equations are then written as

$$\frac{d\mathbf{M}(t)}{dt} = (\mathbf{\Omega}(t) + \mathbf{\Lambda} + \mathbf{\Gamma} + \mathbf{\Xi})\mathbf{M}(t) + \mathbf{D}(t), \quad [4]$$

where

$$\mathbf{\Omega}(t) = \begin{bmatrix} 0 & \gamma\mathbf{G}(t)\cdot\mathbf{r} + 2\pi\Delta f & -\gamma B_{1,y}(t) & 0 \\ -(\gamma\mathbf{G}(t)\cdot\mathbf{r} + 2\pi\Delta f) & 0 & \gamma B_{1,x}(t) & 0 \\ \gamma B_{1,y}(t) & -\gamma B_{1,x}(t) & 0 & 0 \\ 0 & 0 & 0 & -W(\Delta(t), t) \end{bmatrix},$$

$$\mathbf{\Lambda} = \begin{bmatrix} 0 & 0 & 0 & 0 \\ 0 & 0 & 0 & 0 \\ 0 & 0 & -k^f & k^s \\ 0 & 0 & k^f & -k^s \end{bmatrix}, \mathbf{\Gamma} = \begin{bmatrix} -\frac{F}{\lambda} & 0 & 0 & 0 \\ 0 & -\frac{F}{\lambda} & 0 & 0 \\ 0 & 0 & -\frac{F}{\lambda} & 0 \\ 0 & 0 & 0 & 0 \end{bmatrix}, \mathbf{\Xi} = \begin{bmatrix} -\frac{1}{T_2^f} & 0 & 0 & 0 \\ 0 & -\frac{1}{T_2^f} & 0 & 0 \\ 0 & 0 & -\frac{1}{T_1^f} & 0 \\ 0 & 0 & 0 & -\frac{1}{T_1^s} \end{bmatrix}, \quad [5]$$

$$\text{and } \mathbf{D}(t) = \begin{bmatrix} 0 \\ 0 \\ \left(\frac{1}{T_1^f} + \frac{F}{\lambda}\right) M_0^f + s(t) \\ \frac{1}{T_1^s} M_0^s \end{bmatrix}.$$

The matrix $\mathbf{\Omega}(t)$ describes evolution due to gradients, off-resonance (no separate free precession operator), and RF pulses, $\mathbf{\Lambda}$ describes evolution due to exchange, $\mathbf{\Gamma}$ describes evolution due to the clearance of transverse and longitudinal magnetization by venous flow, $\mathbf{\Xi}$ describes evolution due to relaxation, and $\mathbf{D}(t)$ is the time-dependent equilibrium magnetization. M_0^f and M_0^s denote the equilibrium magnetizations for the liquid and semisolid pools, respectively, k^f and k^s refer to forward

($f \rightarrow s$) and reverse ($s \rightarrow f$) exchange rates between two compartments in sec^{-1} and the fundamental rate constant k relates them by $k = k^f/M_0^s = k^s/M_0^f$. The semisolid pool fraction f is defined as $f = M_0^s/M_0^f$ and relates forward and reverse exchange rates by $k^s = k^f/f$. The instantaneous saturation rate $W(\Delta(t), t)$ describes the effect of pulsed irradiation (frequency offset Δ_{offset}) on the longitudinal magnetization of the semisolid protons (8) and is defined as $W(\Delta(t), t) = \pi\gamma^2\|\mathbf{B}_1(t)\|_2^2 G(\Delta(t), T_2^s)$ in rad/sec, where $G(\Delta(t), T_2^s)$ is the absorption lineshape of the semisolid pool in sec and $\Delta(t) \triangleq \Delta_{\text{offset}} - (\gamma\mathbf{G}(t)\cdot\mathbf{r} + 2\pi\Delta f)$ is the adjusted time-dependent frequency offset to account for local field shifts by gradient fields and off-resonance on the absorption response.

2.3 Extended Matrix Formalism

The Bloch equations can be efficiently solved using Jaynes' matrix formalism (32). Here we derive evolution operators for the BMF equations. We assume that the duration of a signal evolution is divided into N timesteps and each timestep is associated with an RF pulse (x and y components) ($\mathbf{B}_i$), gradient ($\mathbf{G}_i$), start time (t_i), measurement time (ξ_i), and duration (τ_i) of the timestep. Assuming a piecewise constant RF pulse and $\mathbf{G}(t)$ over each timestep, the magnetization evolves due to gradients and RF pulses as $\mathbf{M}(t_i + \tau_i) = \mathbf{R}_i\mathbf{M}(t_i)$ where $\mathbf{R}_i = \exp(\boldsymbol{\Omega}(t_i)\tau_i)$. This operator $\mathbf{R}_i$ consists of a rotation matrix $\mathbf{R}(\mathbf{u}_i, \theta_i)$ about the axis $\mathbf{u}_i = [u_x, u_y, u_z]^{\mathrm{T}}$ of an angle θ_i for the free water and a saturation term for the semisolid pool:

$$\mathbf{R}_i = \begin{bmatrix} \mathbf{R}(\mathbf{u}_i, \theta_i) & \mathbf{0} \\ \mathbf{0} & \exp(-W(\Delta(t_i), t_i)\tau_i) \end{bmatrix}, \qquad [6]$$

where

$$\mathbf{R}(\mathbf{u}, \theta) = \begin{bmatrix} \cos\theta + u_x^2(1-\cos\theta) & u_x u_y(1-\cos\theta) - u_z\sin\theta & u_x u_z(1-\cos\theta) + u_y\sin\theta \\ u_y u_x(1-\cos\theta) + u_z\sin\theta & \cos\theta + u_y^2(1-\cos\theta) & u_y u_z(1-\cos\theta) - u_x\sin\theta \\ u_z u_x(1-\cos\theta) - u_y\sin\theta & u_z u_y(1-\cos\theta) + u_x\sin\theta & \cos\theta + u_z^2(1-\cos\theta) \end{bmatrix}, \qquad [7]$$

$\theta_i = \gamma\tau_i\|\mathbf{B}(t_i)\|_2$, $\mathbf{B}(t_i) = [B_{1,x}(t_i), B_{1,y}(t_i), \mathbf{G}(t_i)\cdot\mathbf{r} + 2\pi\Delta f/\gamma]^T$, and $\mathbf{u}_i = \mathbf{B}(t_i)/\|\mathbf{B}(t_i)\|_2$. Note that we use a left-handed convention for the rotation in the right-handed coordinate system. The

general solution to the temporal evolution of the magnetization due to exchange, clearance, and relaxation is

$$\mathbf{M}(t_i+\tau_i) = e^{(\mathbf{\Lambda}+\mathbf{\Gamma}+\mathbf{\Xi})\tau_i}\mathbf{M}(t_i) + \int_{t_i}^{t_i+\tau_i} e^{(\mathbf{\Lambda}+\mathbf{\Gamma}+\mathbf{\Xi})(t_i+\tau_i-\tau)}\mathbf{D}(\tau)d\tau. \quad [8]$$

Using a piecewise constant approximation of $s(t)$ over duration τ_i, i.e., $\mathbf{D}(\tau) = \mathbf{D}(t_i)$ for $t_i \le \tau \le t_i + \tau_i$ and this formula $\int_0^t e^{\mathbf{A}\tau}d\tau = (e^{\mathbf{A}t} - \mathbf{I})\mathbf{A}^{-1}$, we simplify the integral equation and obtain a closed-form expression as

$$\mathbf{M}(t_i+\tau_i) \cong e^{(\mathbf{\Lambda}+\mathbf{\Gamma}+\mathbf{\Xi})\tau_i}\mathbf{M}(t_i) + \left(e^{(\mathbf{\Lambda}+\mathbf{\Gamma}+\mathbf{\Xi})\tau_i} - \mathbf{I}\right)(\mathbf{\Lambda}+\mathbf{\Gamma}+\mathbf{\Xi})^{-1}\mathbf{D}(t_i). \quad [9]$$

With the second approximation that relaxation and exchange can be decoupled (40,41), we get $\exp((\mathbf{\Lambda}+\mathbf{\Gamma}+\mathbf{\Xi})\tau_i) \cong \exp(\mathbf{\Lambda}\tau_i)\cdot\exp(\mathbf{\Gamma}\tau_i)\cdot\exp(\mathbf{\Xi}\tau_i) = \mathbf{A}(\tau_i)\mathbf{C}(\tau_i)\mathbf{E}(\tau_i)$ where exchange $\mathbf{A}(\tau_i)$, clearance $\mathbf{C}(\tau_i)$, and relaxation $\mathbf{E}(\tau_i)$ operators are defined as

$$\mathbf{A}(\tau_i) = \frac{1}{f+1}\begin{bmatrix} f+1 & 0 & 0 & 0 \\ 0 & f+1 & 0 & 0 \\ 0 & 0 & 1+f\exp(-(f+1)k^s\tau_i) & 1-\exp(-(f+1)k^s\tau_i) \\ 0 & 0 & f-f\exp(-(f+1)k^s\tau_i) & f+\exp(-(f+1)k^s\tau_i) \end{bmatrix},$$
$$\mathbf{C}(\tau_i) = \begin{bmatrix} e^{-\tau_i F/\lambda} & 0 & 0 & 0 \\ 0 & e^{-\tau_i F/\lambda} & 0 & 0 \\ 0 & 0 & e^{-\tau_i F/\lambda} & 0 \\ 0 & 0 & 0 & 1 \end{bmatrix}, \text{ and } \mathbf{E}(\tau_i) = \begin{bmatrix} e^{-\tau_i/T_2^f} & 0 & 0 & 0 \\ 0 & e^{-\tau_i/T_2^f} & 0 & 0 \\ 0 & 0 & e^{-\tau_i/T_1^f} & 0 \\ 0 & 0 & 0 & e^{-\tau_i/T_1^s} \end{bmatrix}. \quad [10]$$

Therefore, the temporal evolution in the absence of RF for the BMF equations can be approximated as

$$\mathbf{M}(t_i+\tau_i) = \mathbf{A}(\tau_i)\mathbf{C}(\tau_i)\mathbf{E}(\tau_i)\mathbf{M}(t_i) + \left(\mathbf{I} - \mathbf{A}(\tau_i)\mathbf{C}(\tau_i)\mathbf{E}(\tau_i)\right) * \cdots$$
$$\cdots \begin{bmatrix} 0 \\ 0 \\ \left(\frac{1+T_1^s k^s}{1+T_{1app}\,k^f+T_1^s k^s}\right)\left(M_0^f + s(t_i)T_{1app}\right) + \left(\frac{T_{1app}\,k^s}{1+T_{1app}\,k^f+T_1^s k^s}\right)M_0^s \\ \left(\frac{T_1^s k^f}{1+T_{1app}\,k^f+T_1^s k^s}\right)\left(M_0^f + s(t_i)T_{1app}\right) + \left(\frac{1+T_{1app}\,k^f}{1+T_{1app}\,k^f+T_1^s k^s}\right)M_0^s \end{bmatrix}, \quad [11]$$

where $T_{1app} = 1/T_1^f + F/\lambda$ is the apparent T_1 relaxation time for the (liquid pool) longitudinal magnetization. Note that with the first approximation, the amount of labeled blood over a timestep is estimated by multiplying the ASL bolus signal $s(t)$ at the start time t_i of the i^{th} timestep with duration τ_i (See **Figure 1**). This approximation is valid provided that the T1 decay of labeled blood is slow (or negligible) over the duration of each timestep. For the BMF equations without MT effects (herein denoted BF equations) we do not need the second approximation since $\mathbf{\Gamma\Xi} = \mathbf{\Xi\Gamma}$. The temporal evolution in the absence of RF for the BF equations can be obtained by setting $M_0^s = 0, k^f = 0, k^s = 0, \mathbf{A}(\tau_i) = \mathbf{I}$ in Equation 10. Note also that without considering MT effects, for each timestep, liquid pool protons (tissue water) relax with a new time-dependent pseudo equilibrium magnetization: $M_0^f + s(t_i)T_{1app}$.

Using the extended matrix formalism, the magnetizations in the i^{th} timestep of **Figure 1** can be expressed as:

$$\text{Initialization: } \mathbf{M}_a[i] = \mathbf{M}_d[i-1] \quad [12]$$

$$\text{RF excitation: } \mathbf{M}_b[i] = \mathbf{R}_i\mathbf{M}_a[i] \quad [13]$$

$$\mathbf{M}_c[i] = \mathbf{A}(\xi_i)\mathbf{C}(\xi_i)\mathbf{E}(\xi_i)\mathbf{M}_b[i] + \left(\mathbf{I} - \mathbf{A}(\xi_i)\mathbf{C}(\xi_i)\mathbf{E}(\xi_i)\right)[0,0,\dots\left(M_0^f + s(t_i)T_{1app}\right)\dots]^T \quad [14]$$

$$\begin{aligned}\mathbf{M}_d[i] &= \mathbf{A}(\tau_i - \xi_i)\mathbf{C}(\tau_i - \xi_i)\mathbf{E}(\tau_i - \xi_i)\mathbf{M}_c[i] \\ &+(\mathbf{I} - \mathbf{A}(\tau_i - \xi_i)\mathbf{C}(\tau_i - \xi_i)\mathbf{E}(\tau_i - \xi_i))[0,0,\dots\left(M_0^f + s(t_i)T_{1app}\right)\dots]^T\end{aligned} \quad [15]$$

The magnetization vector $\mathbf{M}_c[i]$ at ξ_i for each timestep is collected and this computation is performed from the first to the last timestep.

3. METHODS

All simulations were performed using MATLAB R2018a (The MathWorks, Natick, MA, USA) on a PC equipped with one 1.60 GHz 4-core Intel i5-8250U CPU and 20 GB of random-access memory.

3.1 Numerical Validation against single delay PASL and PCASL

The proposed numeric approximation was compared with GKM for single-compartment kinetics with pulsed labeling and pseudo-continuous labeling. For both labeling methods, recommended labeling parameters were obtained from the recent consensus paper by Alsop et al. (1). PASL/PCASL labeling parameters were T_D = 700 msec, T_W = 800/1800 msec, and α (labeling efficiency) = 0.98/0.85. When MT effects are not considered, superscripts are omitted. Simulation parameters for a typical gray matter voxel were F = 0.6 mL/g/min, T_1/T_{1b} = 1200/1650 msec, M_0 = 1, λ = 0.9, $\alpha_0 = 2\alpha$ (inversion). For both labeling methods, the labeling pulse was applied at 0 sec. The duration of signal evolution was 4 sec. The number N of timesteps was calculated as $N = \lfloor T/\tau \rfloor$, where T is the total duration and τ is the timestep used for numeric approximation. ASL signals were calculated with two timesteps τ = 3 and τ = 35 msec. The shorter timestep, 3 msec, was chosen based on its use as the imaging TR in cardiac ASL (42). The longer timestep, 35 msec, was chosen based on its use as the imaging TR in MRF-ASL (37). For the numeric approximation, control and label signals without and with labeling were first calculated at measurement times $\{\xi_i\}_{i=1}^{N} = \{\tau_i\}_{i=1}^{N} = \tau$, and then a difference between these signals was set to the PASL/PCASL signal. For GKM, PASL and PCASL signals were calculated by evaluating Equations 3 and 5 of Buxton et al. (6), respectively.

3.2 Numerical Accuracy

We investigated the effect of the timestep (τ) on the accuracy of the approximation. We tested 500 timesteps linearly spaced from 0 to 50 msec in increments of 0.1 msec. ASL signals with inversion labeling were generated with GKM (denoted $\Delta \mathrm{M}_{\mathrm{GKM}}(\mathrm{t})$) and the numeric approximation (denoted $\Delta \mathrm{M}_{\mathrm{numeric}}(\mathrm{t})$) while sweeping parameters for transit delay T_D and bolus duration T_W. The range of each parameter and fixed parameters were adapted from the recent consensus paper (1) and listed in **Supporting Information Table S1**. The accuracy of the numeric approximation was assessed using two metrics: (1) overall normalized root-mean-square error $(\mathrm{NRMSE}) = \|\Delta \mathrm{M}_{\mathrm{GKM}}(\mathrm{t}) - \Delta \mathrm{M}_{\mathrm{numeric}}(\mathrm{t})\|_2 / \|\Delta \mathrm{M}_{\mathrm{GKM}}(\mathrm{t})\|_2$, and (2) maximum deviation between GKM and the numeric approximation (Max Deviation) $= \max |\Delta \mathrm{M}_{\mathrm{GKM}}(\mathrm{t}) - \Delta \mathrm{M}_{\mathrm{numeric}}(\mathrm{t})|$. Blood flow F was not chosen as a sweeping parameter because a change in blood flow does not affect the NRMSE but linearly affects the max deviation. Simulations of two perfusion values (0.3 and 0.6 mL/g/min) for gray matter were performed. The effects of a change in spin-lattice relaxation T_1 on the two metrics are negligible and therefore spin-lattice relaxation T_1 was omitted.

3.3 Numerical Validation against spASL and MRF-ASL

To demonstrate the generality of the framework to various unconventional sequences, we validated the numeric approximation without MT effects against the customized signal expressions of spASL (34,35,43) and MRF-ASL (36). Each sequence's own customized signal expression is analytically derived with GKM and described in a respective reference in detail.

For spASL, theoretical signal evolutions in Figure 1 of Capron et al. (34) were reproduced using the numeric approximation with TR = τ = 10 msec. A spASL pulse sequence consists of 4 phases: imaging during label, recovery, imaging during control, and recovery. The duration of an acquisition phase is denoted as tp and the recovery delay as RD. These 4 phases are repeated for Nlines (number of k-space lines). Four spASL simulations of the mouse heart with different imaging parameters (Nlines, tp, RD) were performed assuming no transit delay and T1 relaxation of arterial magnetization. Other fixed parameters were T_1= 1400 msec, θ= 8°, F = 6 mL/g/min, λ = 0.95, $\alpha_0 = 2\beta$ = 1 (saturation). The numeric approximation incorporates perfect spoiling at the end of TR to simulate FLASH-readouts.

For MRF-ASL, a simulation study of Su et al. (36) was reproduced with τ = 1 msec. An MRF-ASL pulse sequence consists of randomly ordered control and label scans, each comprising a period of pulsed labeling and an acquisition without a post labeling delay. We used 30 TRs (a total of 30 scans) for a clear illustration of signal evolutions. A labeling duration time series was generated with a half-cycle cosine function gradually decreasing from 450 to 72 msec. A pseudo-randomized order of label and control was used. Other fixed parameters were θ= 40°, F = 0.6 mL/g/min, $T_D/T_1/T_{1b}$= 1000/1200/1650 msec, M_0 = 1, λ = 0.9, $\alpha_0 = 2\alpha$ = 2 (inversion). A single compartment model consisting of a tissue compartment without a pass-through artery compartment was used for both GKM and the numeric approximation. The T2 decay of transverse magnetization was not considered when deriving theoretical signal evolutions with GKM. Off-resonance (Δf = 30 Hz) and T_2 effects (T_2 = 80 msec) were simulated with the numeric approximation.

3.4 Modeling Flow and MT effects in bSSFP and SPGR

We demonstrated simultaneous modeling of flow, T_2, and MT effects in simulations using steady-state imaging sequences: bSSFP (29,44) and SPGR (45). Steady-state bSSFP and SPGR signals were obtained at flip angles from 1° to 80° in increments of 1°. We assumed instantaneous RF rotation and thus the mean saturation rate averaged over TR was used (8,40,41). Signals for four cases were generated: 1) no MT, no flow, 2) no MT, flow, 3) MT, no flow, and 4) MT, flow. The second approximation was compared with the exact evaluation (i.e., matrix exponential). Simulation parameters (white matter at 1.5T) were obtained from Gloor et al. (29): M_0^f = 1, T_1^f = 585 msec, T_2^f = 81

msec, f = 0.157, k^f = 4.45, T_1^s = 1000 msec, T_2^s = 12μsec, G = 14 μsec, and F = 4 mL/g/min, λ = 0.9, τ = 4 μsec; For bSSFP, pulse duration = 230 μsec, TR = 2.92 msec, TE = TR/2; For SPGR, pulse duration = 200 μsec, TR = 5 msec, TE = TR/2.

4. RESULTS

Figure 2 compares PASL and PCASL signals obtained with GKM and the numeric approximation using fixed timesteps of 3 and 35 msec. For timesteps of 3 and 35 msec, the maximum deviations between GKM and the numeric approximation were 0.002% and 0.05% for PASL (**2e, 2f**), and 0.002% and 0.042% for PCASL (**2g, 2h**), respectively.

Figure 3 shows NRMSE, maximum deviation, and computation time as a function of the timestep (mean ± one standard deviation) for PASL and PCASL with tissue blood flow of 0.6 mL/g/min (**Supporting Information Figure S1** for tissue blood flow of 0.3 mL/g/min). For both labeling methods, the NRMSE increased approximately linearly with respect to timestep (**3a, 3b**). The max deviation also increased linearly with respect to timestep (**3c, 3d**). The mean (σ) and standard deviation (μ) of the max deviation increased linearly with respect to tissue blood flow, but the coefficient of variation ($CV = \sigma/\mu * 100\%$) remained the same (**3c**, **S1c**). The linear slope of the NRMSE for PASL was higher than that for PCASL. A larger standard deviation in the NRMSE for PASL was observed compared with PCASL. The linear slope of the maximum deviation for PASL was lower than that for PCASL while a similar standard deviation was observed for both labeling methods. For 1 and 35 msec, the mean computation times were 4.60 and 0.14 msec for PASL, and 4.42 and 0.14 msec for PCASL, respectively.

Figure 4 compares the theoretical signal evolutions for spASL obtained with a customized signal expression and the numeric approximation. This example demonstrates the numeric approximation can model the effects of flow under imaging RF pulses. For all cases, the maximum signal difference was < 0. 97%.

Figure 5 compares the MRF-ASL signal evolutions obtained with GKM and the numeric approximation. The numeric approximation shows excellent agreement with GKM with a maximum signal difference of 0.002%. The numeric approximation deviates from GKM when T_2 effects and off-resonance are modeled. When a spoiling gradient is used after each acquisition to dephase transverse magnetization, T_2 effects would not be a concern, and the numerical simulation results would be consistent with that from GKM.

Supporting Information Figure S2 shows steady-state bSSFP and SPGR signals for white matter at 1.5T calculated for four combinations of MT and flow effects. The constant un-labeled inflow causes an increase in both steady-state bSSFP and SPGR signals. Signals obtained with the second approximation shows excellent agreement with those obtained with exact evaluation. This justifies the use of the second approximation to replace computationally expansive evaluation of the matrix exponential.

5. DISCUSSION

We have demonstrated a numerical approximation to the general kinetic model for ASL quantification. We have also characterized the tradeoff between accuracy and computation time, through the selection of the timing interval. This numeric approximation is first validated against GKM for PASL and PCASL, and further validated against customized signal expressions of non-standard ASL pulse sequences, spASL and MRF-ASL. The numerical approach provides an excellent approximation to GKM as long as the timestep is sufficiently small (Figures 2 and 3). The important feature of the numerical approach is the piecewise constant approximation of blood inflow between excitation 'i' and 'i+1'. As the distance between consecutive excitations becomes longer, the error in the estimation of the amount of labeled blood increases.

One advantage of the proposed approach is that both transient-state and steady-state signal evolutions can be generated in the presence of flow, T_2 effects, off-resonance, MT effects, and irregular timing of RF labeling. This key feature 1) makes it applicable to highly challenging ASL scenarios, including cardiac ASL which suffers from irregular timing due to ECG-gating and heart variability, and 2) enables more flexible and irregular quantitative ASL experiments such as recent attempts at MRF-ASL. Another advantage of the proposed approach is that dispersion effects can be easily incorporated, because $s(t)$ can be numerical functions.

There are several possible extensions to this work. Although we demonstrate simultaneous modeling of MT effects and ASL perfusion in simulation studies, experimental verification still remain. For non-balanced gradient-echo sequences, signal evolutions can be efficiently predicted using the extended phase graph (EPG) framework (46–48) instead of time-intensive isochromat-based Bloch simulations. Incorporating the proposed modeling approach to the EPG framework could provide time-efficient computation of ASL signal evolutions for a broad range of pulse sequences. Recent progress in MRF-ASL might be also benefit from this work, particularly (and interestingly) those utilizing deep

learning approaches. The proposed numerical approximation with matrix formalism can potentially be combined with deep learning to further improve quantification of flow (49-51).

6. CONCLUSION

We demonstrate and validate an extension to the Bloch equations, termed Bloch-McConnell-Flow equations, which can simultaneously model the effects of flow with various other effects. We also demonstrate and validate an extension to Jaynes' matrix formalism to provide a numeric approximation to these BMF equations. In simulation, the proposed approach provides an arbitrarily accurate approximation to the general kinetic model. A single timestep tuning parameter allows one to tradeoff accuracy for computational speed. The proposed approach will enable quantification of transient-state ASL and ASL with irregular timing of RF labeling and/or severe off-resonance, which are challenging for current techniques.

Data Availability Statement: The code and data that support the findings of this study are openly available in GitHub at https://www.github.com/usc-mrel/Bloch_Flow_MT.

References

1. Alsop DC, Detre JA, Golay X, et al. Recommended implementation of arterial spin-labeled perfusion MRI for clinical applications: A consensus of the ISMRM perfusion study group and the European consortium for ASL in dementia. Magn. Reson. Med. 2015;73:102–16 doi: 10.1002/mrm.25197.

2. Odudu A, Nery F, Harteveld AA, et al. Arterial spin labelling MRI to measure renal perfusion: a systematic review and statement paper. Nephrol. Dial. Transplant 2018 doi: 10.1093/ndt/gfy180.

3. Kober F, Jao T, Troalen T, Nayak KS. Myocardial arterial spin labeling. J. Cardiovasc. Magn. Reson. 2016;18:1–16 doi: 10.1186/s12968-016-0235-4.

4. Williams DS, Detre JA, Leigh JS, Koretsky AP. Magnetic resonance imaging of perfusion using spin inversion of arterial water. Proc. Natl. Acad. Sci. U. S. A. 1992;89:212–6.

5. Detre JA, Leigh JS, Williams DS, Koretsky AP. Perfusion imaging. Magn. Reson. Med. 1992;23:37–45 doi: 10.1002/mrm.1910230106.

6. Buxton RB, Frank LR, Wong EC, Siewert B, Warach S, Edelman RR. A general kinetic model for quantitative perfusion imaging with arterial spin labeling. Magn. Reson. Med. 1998 doi: 10.1002/mrm.1910400308.

7. Sled JG, Pike GB. Quantitative Interpretation of Magnetization Transfer in Spoiled Gradient Echo MRI Sequences. 2000;36:24–36 doi: 10.1006/jmre.2000.2059.

8. Graham SJ, Henkelman RM. Understanding pulsed magnetization transfer. J. Magn. Reson. Imaging 1997 doi: 10.1002/jmri.1880070520.

9. Henkelman RM, Stanisz GJ, Graham SJ. Magnetization transfer in MRI : a review. 2001:57–64 doi: 10.1002/nbm.683.

10. Alsop DC, Detre JA. Reduced transit-time sensitivity in noninvasive magnetic resonance imaging of human cerebral blood flow. J. Cereb. Blood Flow Metab. 1996;16:1236–1249 doi: 10.1097/00004647-199611000-00019.

11. Zhang W, Williams DS, Detre JA, Koretsky AP. Measurement of brain perfusion by volume-localized NMR spectroscopy using inversion of arterial water spins: Accounting for transit time and cross-relaxation. Magn. Reson. Med. 1992 doi: 10.1002/mrm.1910250216.

12. Zhang W, Williams DS, Koretsky AP. Measurement of rat brain perfusion by NMR using spin labeling of arterial water: In vivo determination of the degree of spin labeling. Magn. Reson. Med. 1993 doi: 10.1002/mrm.1910290323.

13. Zhang W, Silva AC, Williams DS, Koretsky AP. NMR Measurement of Perfusion Using Arterial Spin Labeling Without Saturation of Macromolecular Spins. Magn. Reson. Med. 1995 doi:

10.1002/mrm.1910330310.
14. Pekar J, Jezzard P, Roberts DA, Leigh JS, Frank JA, McLaughlin AG. Perfusion imaging with compensation for asymmetric magnetization transfer effects. Magn. Reson. Med. 1996 doi: 10.1002/mrm.1910350110.
15. McLaughlin AC, Ye FQ, Pekar JJ, Santha AKS, Frank JA. Effect of magnetization transfer on the measurement of cerebral blood flow using steady-state arterial spin tagging approaches: A theoretical investigation. Magn. Reson. Med. 1997 doi: 10.1002/mrm.1910370406.
16. Bauer WR, Hiller KH, Roder F, Rommel E, Ertl G, Haase A. Magnetization exchange in capillaries by microcirculation affects diffusion-controlled spin-relaxation: A model which describes the effect of perfusion on relaxation enhancement by intravascular contrast agents. Magn. Reson. Med. 1996;35:43–55 doi: 10.1002/mrm.1910350107.
17. St Lawrence KS, Frank JA, McLaughlin AC. Effect of restricted water exchange on cerebral blood flow values calculated with arterial spin tagging: A theoretical investigation. Magn. Reson. Med. 2000 doi: 10.1002/1522-2594(200009)44:3<440::AID-MRM15>3.0.CO;2-6.
18. Parkes LM, Tofts PS. Improved accuracy of human cerebral blood perfusion measurements using arterial spin labeling: Accounting for capillary water permeability. Magn. Reson. Med. 2002 doi: 10.1002/mrm.10180.
19. Gallichan D, Jezzard P. Modeling the effects of dispersion and pulsatility of blood flow in pulsed arterial spin labeling. Magn. Reson. Med. 2008;60:53–63 doi: 10.1002/mrm.21654.
20. Kazan SM, Chappell MA, Payne SJ. Modeling the effects of flow dispersion in arterial spin labeling. IEEE Trans. Biomed. Eng. 2009;56:1635–1643 doi: 10.1109/TBME.2009.2016977.
21. Chappell MA, Woolrich MW, Kazan S, Jezzard P, Payne SJ, MacIntosh BJ. Modeling dispersion in arterial spin labeling: Validation using dynamic angiographic measurements. Magn. Reson. Med. 2013;69:563–570 doi: 10.1002/mrm.24260.
22. H.C.Torrey. Bloch Equation with Diffusion Terms. Phys. Rev. 1956;104:563–565.
23. Awojoyogbe OB, Dada OM, Faromika OP, Dada OE. Mathematical concept of the Bloch flow equations for general magnetic resonance imaging: A review. Concepts Magn. Reson. Part A Bridg. Educ. Res. 2011 doi: 10.1002/cmr.a.20210.
24. McConnell HM. Reaction rates by nuclear magnetic resonance. J. Chem. Phys. 1958;28:430–431 doi: 10.1063/1.1744152.
25. Zaiss M, Zu Z, Xu J, et al. A combined analytical solution for chemical exchange saturation transfer and semi-solid magnetization transfer. NMR Biomed. 2015;28:217–230 doi: 10.1002/nbm.3237.

26. Woessner DE, Zhang S, Merritt ME, Sherry AD. Numerical solution of the Bloch equations provides insights into the optimum design of PARACEST agents for MRI. Magn. Reson. Med. 2005;53:790–799 doi: 10.1002/mrm.20408.
27. Drobnjak I, Zhang H, Hall MG, Alexander DC. The matrix formalism for generalised gradients with time-varying orientation in diffusion NMR. J. Magn. Reson. 2011 doi: 10.1016/j.jmr.2011.02.022.
28. Portnoy S, Stanisz GJ. Modeling Pulsed Magnetization Transfer. 2007;155:144–155 doi: 10.1002/mrm.21244.
29. Gloor M, Scheffler K, Bieri O. Balanced SSFP. 2008;700:691–700 doi: 10.1002/mrm.21705.
30. Sled JG, Pike GB. Quantitative Imaging of Magnetization Transfer Exchange and Relaxation Properties In Vivo Using MRI. 2001;931:923–931.
31. Henkelman RM, Huang X, Xiang Q -S, Stanisz GJ, Swanson SD, Bronskill MJ. Quantitative interpretation of magnetization transfer. Magn. Reson. Med. 1993 doi: 10.1002/mrm.1910290607.
32. Jaynes ET. Matrix treatment of nuclear induction. Phys. Rev. 1955;98:1099–1105 doi: 10.1103/PhysRev.98.1099.
33. Troalen T, Capron T, Cozzone PJ, Bernard M, Kober F. Cine-ASL: A steady-pulsed arterial spin labeling method for myocardial perfusion mapping in mice. Part I. Experimental study. Magn. Reson. Med. 2013;70:1389–1398 doi: 10.1002/mrm.24565.
34. Capron T, Troalen T, Cozzone PJ, Bernard M, Kober F. Cine-ASL: A steady-pulsed arterial spin labeling method for myocardial perfusion mapping in mice. Part II. Theoretical model and sensitivity optimization. Magn. Reson. Med. 2013;70:1399–1408 doi: 10.1002/mrm.24588.
35. Capron T, Troalen T, Robert B, Jacquier A, Bernard M, Kober F. Myocardial perfusion assessment in humans using steady-pulsed arterial spin labeling. Magn. Reson. Med. 2015;74:990–998 doi: 10.1002/mrm.25479.
36. Su P, Mao D, Liu P, et al. Multiparametric Estimation of Brain Hemodynamics with MR Fingerprinting ASL. 2016;00:1–12 doi: 10.1002/mrm.26587.
37. Wright KL, Jiang Y, Ma D, et al. Estimation of perfusion properties with MR Fingerprinting Arterial Spin Labeling. Magn. Reson. Imaging 2018;50:68–77 doi: 10.1016/j.mri.2018.03.011.
38. Morrison C, Mark Henkelman R. A Model for Magnetization Transfer in Tissues. Magn. Reson. Med. 1995 doi: 10.1002/mrm.1910330404.
39. Detre JA, Zhang W, Roberts DA, et al. Tissue specific perfusion imaging using arterial spin labeling. NMR Biomed. 1994 doi: 10.1002/nbm.1940070112.
40. Gloor M, Scheffler K, Bieri O. Quantitative magnetization transfer imaging using balanced SSFP.

Magn. Reson. Med. 2008 doi: 10.1002/mrm.21705.
41. Gloor M, Scheffler K, Bieri O. Nonbalanced SSFP-Based Quantitative Magnetization Transfer Imaging. 2010;156:149–156 doi: 10.1002/mrm.22331.
42. Zun G, Wong EC, Nayak KS. Assessment of myocardial blood flow (MBF) in humans using arterial spin labeling (ASL): Feasibility and noise analysis. Magn. Reson. Med. 2009;62:975–983 doi: 10.1002/mrm.22088.
43. Xu J, Qin Q, Wu D, et al. Steady pulsed imaging and labeling scheme for noninvasive perfusion imaging. Magn. Reson. Med. 2016;75:238–248 doi: 10.1002/mrm.25641.
44. Bieri O, Scheffler K. On the Origin of Apparent Low Tissue Signals in Balanced SSFP. 2006;1074:1067–1074 doi: 10.1002/mrm.21056.
45. Ou X, Gochberg DF. MT effects and T1 quantification in single-slice spoiled gradient echo imaging. Magn. Reson. Med. 2008;59:835–845 doi: 10.1002/mrm.21550.
46. Hennig J. Echoes -How to Generate , Recognize , Use or Avoid Them in MR-Imaging Sequences Part I : Fundamental and Not So Fundamental Properties of Spin Echoes. 1991:125–143.
47. Weigel M. Extended Phase Graphs : Dephasing , RF Pulses , and Echoes - Pure and Simple. 2015;295:266–295 doi: 10.1002/jmri.24619.
48. Malik SJ, Teixeira RPAG, Hajnal J V. Extended Phase Graph Formalism for Systems With Magnetization Transfer and Exchange. 2018;779:767–779 doi: 10.1002/mrm.27040.
49. Su P, Fan H, Liu P, et al. MR fingerprinting ASL: Sequence characterization and comparison with dynamic susceptibility contrast (DSC) MRI. NMR Biomed. 2020 doi: 10.1002/nbm.4202.
50. Lahiri A, Fessler JA, Hernandez-Garcia L. Optimizing MRF-ASL scan design for precise quantification of brain hemodynamics using neural network regression. Magn. Reson. Med. 2019 doi: 10.1002/mrm.28051.
51. Zhang Q, Su P, Chen Z, Liao Y, Chen S, Guo R, Qi H, Li X, Zhang X, Hu Z, Lu H. Deep learning–based MR fingerprinting ASL ReconStruction (DeepMARS). Magn. Reson. Med. 2020 doi:10.1002/mrm.28166

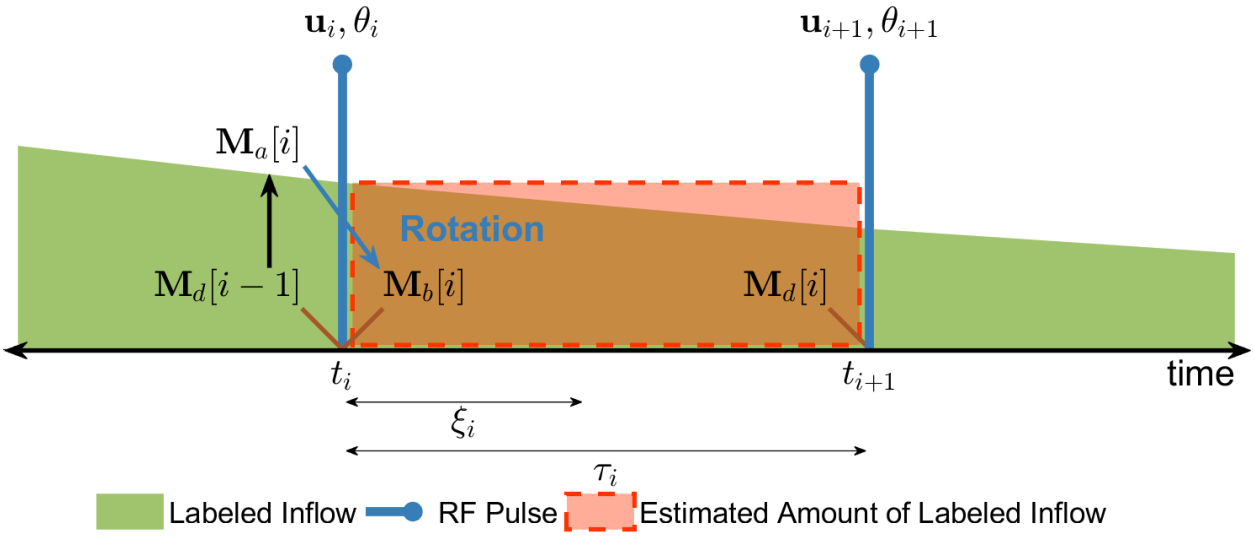

Figure 1. Illustration of the Bloch simulation with flow effects. The extended matrix formalism is demonstrated over a few timesteps. The T1 decay of labeled arterial blood (green) over each timestep is exaggerated. The symbols $\boldsymbol{u}_i/\theta_i/t_i/\xi_i/\tau_i$ indicate rotation axis/rotation angle/start time/measurement time/duration for the i^{th} timestep. Using a piecewise constant approximation, the actual amount of labeled blood over the i^{th} timestep of duration τ_i (green) is overestimated by the area of a rectangle (dashed red box). During each timestep, tissue magnetization relaxes with a new pseudo M_0 term: $M_0 + s(t_i)T_{1app}$. The magnetization of the previous timestep $\mathbf{M}_d[i-1]$ is set to the initial magnetization $\mathbf{M}_a[i]$ for the i^{th} timestep (black arrow). The i^{th} RF excitation yields $\mathbf{M}_b[i]$ (blue arrow) and $\mathbf{M}_d[i]$ is obtained after subsequent applications of relaxation, clearance, and exchange operators. This figure indicates the flexibility of the extended matrix formalism, where each timestep can have varying parameters.

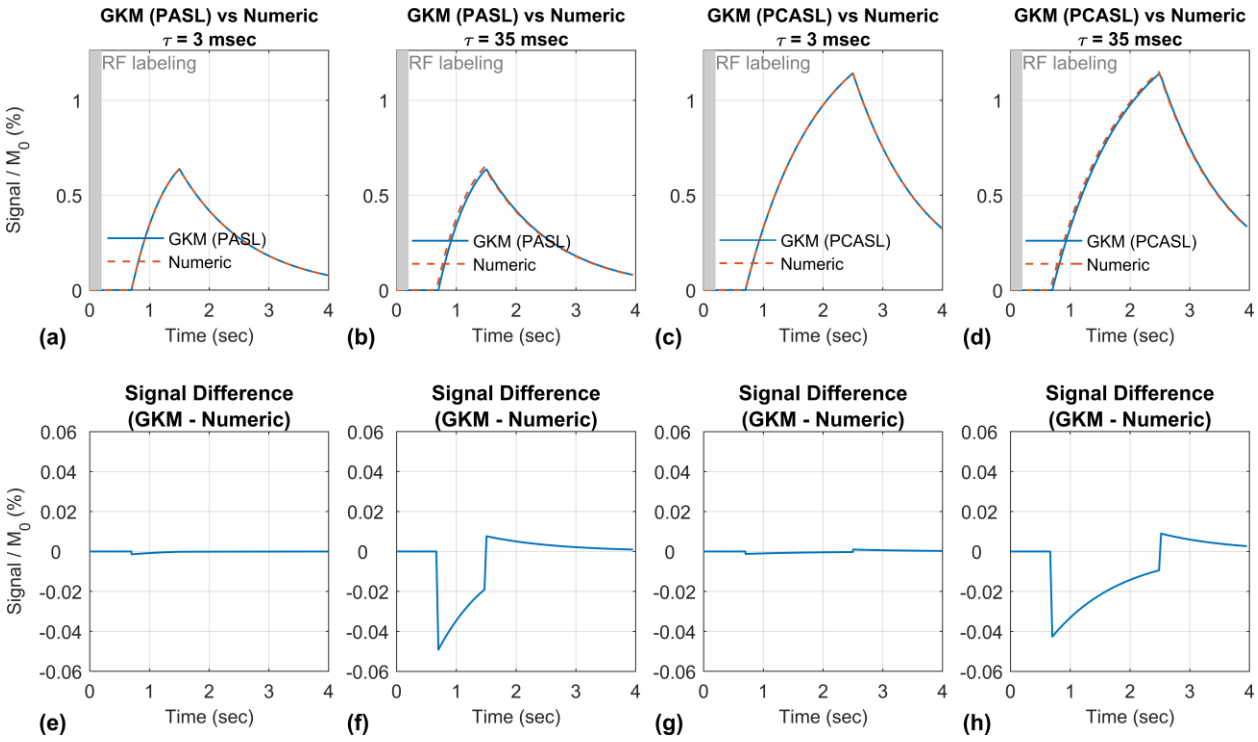

Figure 2. Comparison of simulated PASL and PCASL signals obtained with Buxton's general kinetic model (GKM) and the proposed numeric approximation (numeric). Simulation parameters for PASL/PCASL are F = 0.6 mL/g/min, T_D = 700 msec, T_W = 800/1800 msec, T_1/T_{1b}= 1820/1650 msec, M_0 = 1, λ = 0.9, α (labeling efficiency for PASL/PCASL) = 0.98/0.85, $\alpha_0 = 2\alpha$ (inversion). PASL signals are calculated with single RF labeling and a fixed timestep of (a) τ = 3 and (b) τ = 35 msec. PCASL signals are calculated with a fixed timestep of (c) τ = 3 and (d) τ = 35 msec. Gray bars indicate application of RF labeling. The signal differences between the GKM and the numeric approximation are shown in the 2nd row (e, f, g, and h). In case of $\tau \leq 35$ msec, the maximum signal difference was always < 0.06% for both labeling methods.

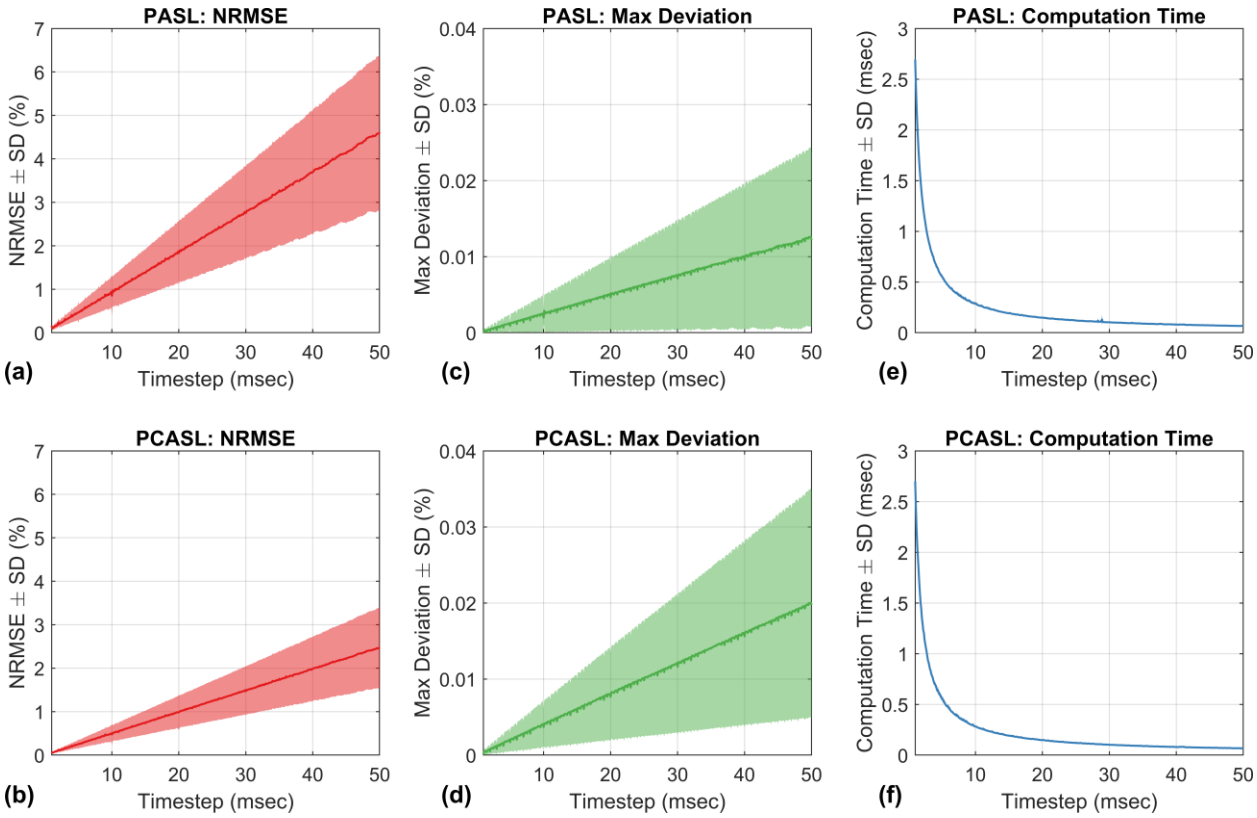

Figure 3. Performance of the proposed approximation depends on the timestep used. Here, we plot NRMSE, max deviation, and computation time as a function of timestep (τ, x-axis). Each plot shows the mean (line) ± one standard deviation (shaded area). (a) NRMSE for PASL. (b) NRMSE for PCASL. (c) Max deviation between GKM and the proposed numeric approximation for PASL. (d) Max deviation between GKM and the proposed numeric approximation for PCASL. (e) Computation time for PASL. (f) Computation time for PCASL. Simulation parameters for both labeling methods are listed in **Supporting Information Table S1**.

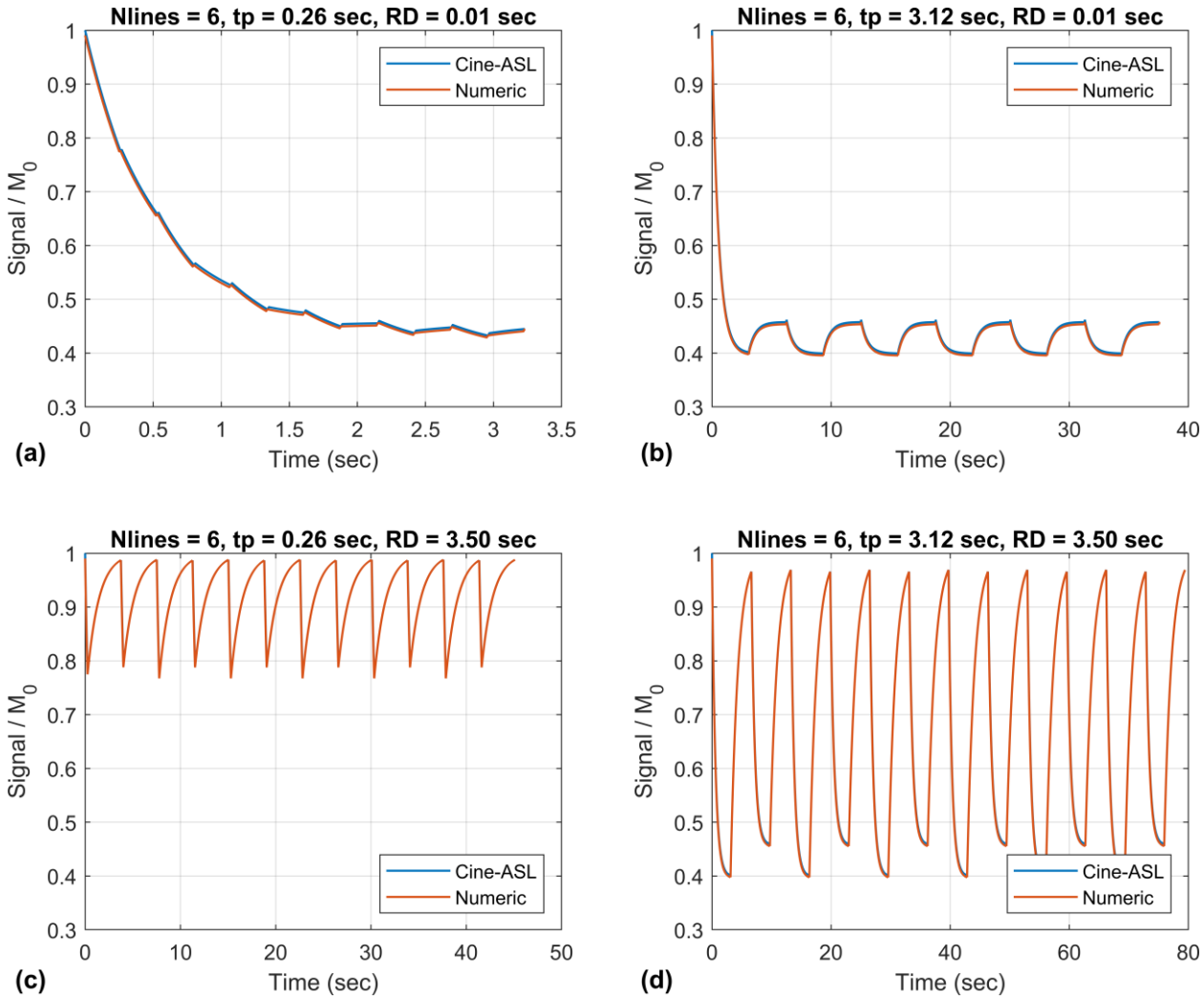

Figure 4. Comparison of theoretical signal evolutions for spASL obtained with a customized signal expression (Cine-ASL) and the proposed numeric approximation (numeric). Figure 1 of Capron et al. (34) is reproduced. The figure shows signal evolutions over 6 (Nlines) repetitions of 4 phases: imaging during label, recovery, imaging during control, and recovery. Signal evolutions for 4 different imaging parameters (RD, t_p) are shown. (a) Short RD = 0.01 sec, short t_p = 0.26 sec, (b) Short RD = 0.01 sec, long t_p = 3.12 sec, (c) Long RD = 3.50 sec, short t_p = 0.26 sec, and (d) Long RD = 0.01 sec, long t_p = 3.12 sec.

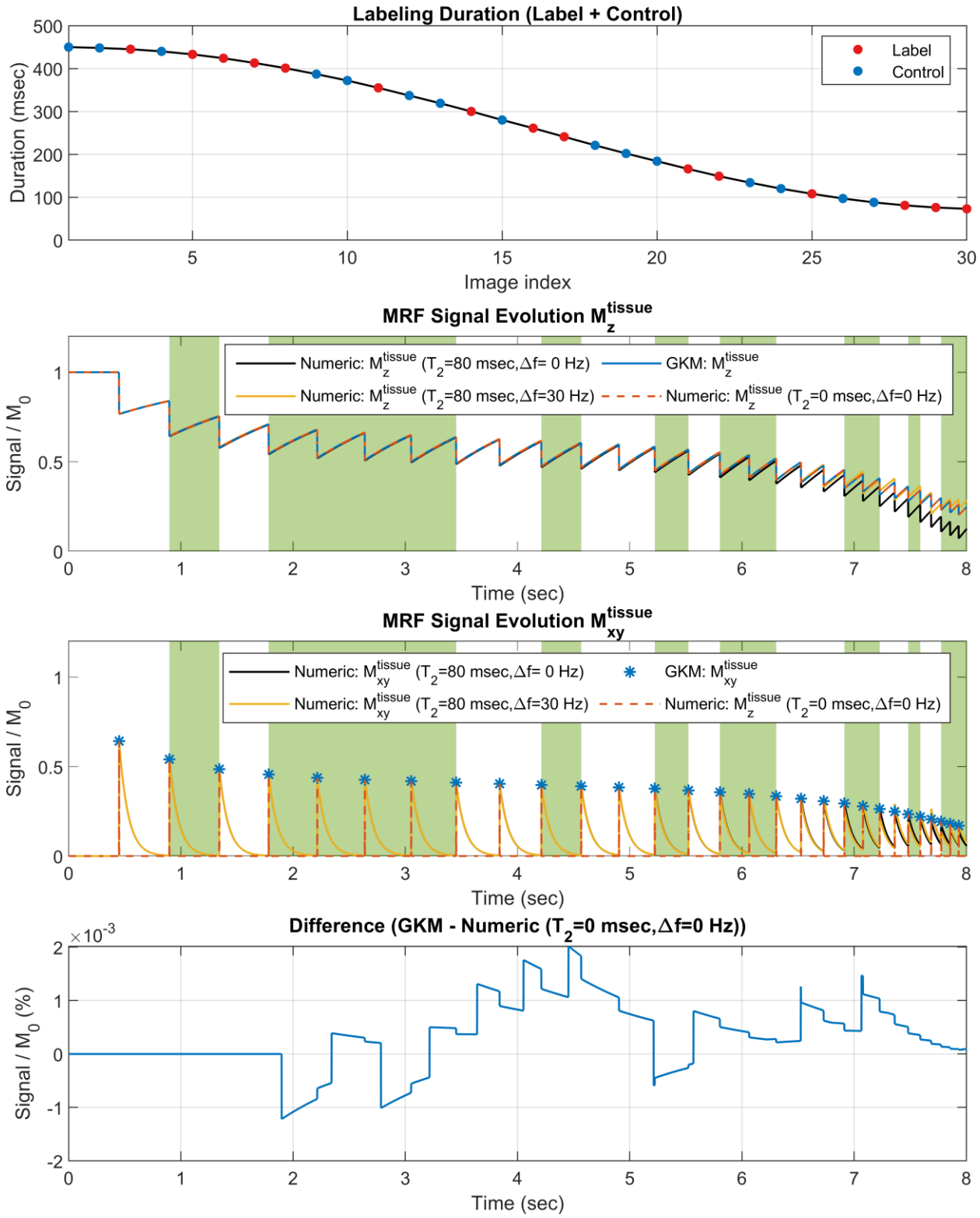

Figure 5. Comparison of MRF-ASL signal evolutions obtained with a customized signal expression based on GKM (GKM) and the proposed numeric approximation (numeric). (1st row) A labeling time series consists of a pseudo-randomized order of label (red) and control (blue) scans. The horizontal axis

represents the duration of a scan in msec. The duration of excitation and acquisition is neglected. The longitudinal (2nd row) and transverse (3rd row) components of MRF-ASL signal evolutions are obtained without MT effects for both GKM and the numeric approximation. Green regions indicate "Label". The numeric approximation calculated without T_2 effects and off-resonance shows excellent agreement with GKM (4th row). The numeric approach can provide more realistic signal evolutions with T_2 effects (black) and with T_2 effects and off-resonance (orange). For short labeling duration ($\leq 3 \cdot T_2$), the transverse magnetization is not completely decayed to zero and starts to affect the longitudinal magnetization of an MRF-ASL signal evolution. When a spoiling gradient is used after each acquisition to dephase transverse magnetization, T_2 effects would not be a concern, and the numerical simulation results would be consistent with that from GKM.

SUPPLEMENTAL FIGURE CAPTIONS

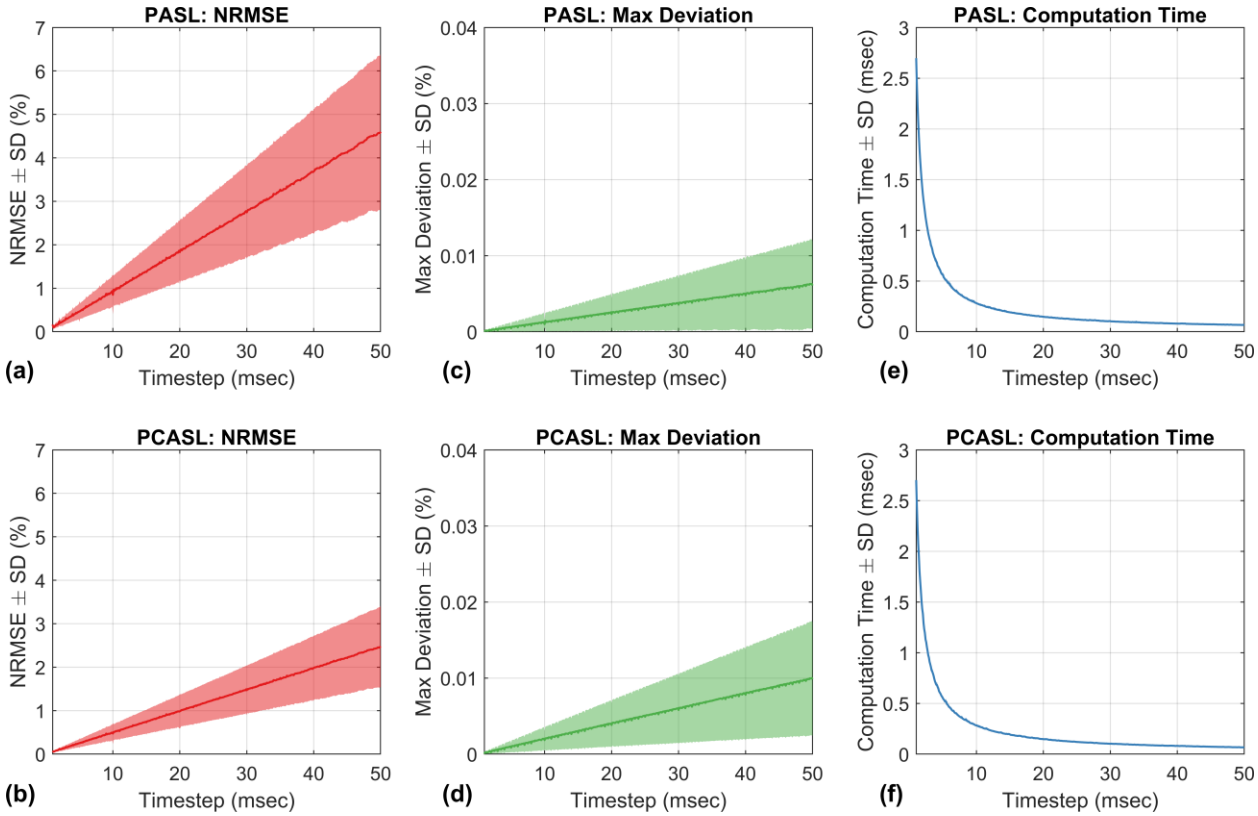

Supporting Information Figure S1. Performance of the proposed approximation for tissue blood flow of 0.3 mL/g/min. (a) NRMSE for PASL. (b) NRMSE for PCASL. (c) Max deviation between GKM and the proposed numeric approximation for PASL. (d) Max deviation between GKM and the proposed numeric approximation for PCASL. (e) Computation time for PASL. (f) Computation time for PCASL.

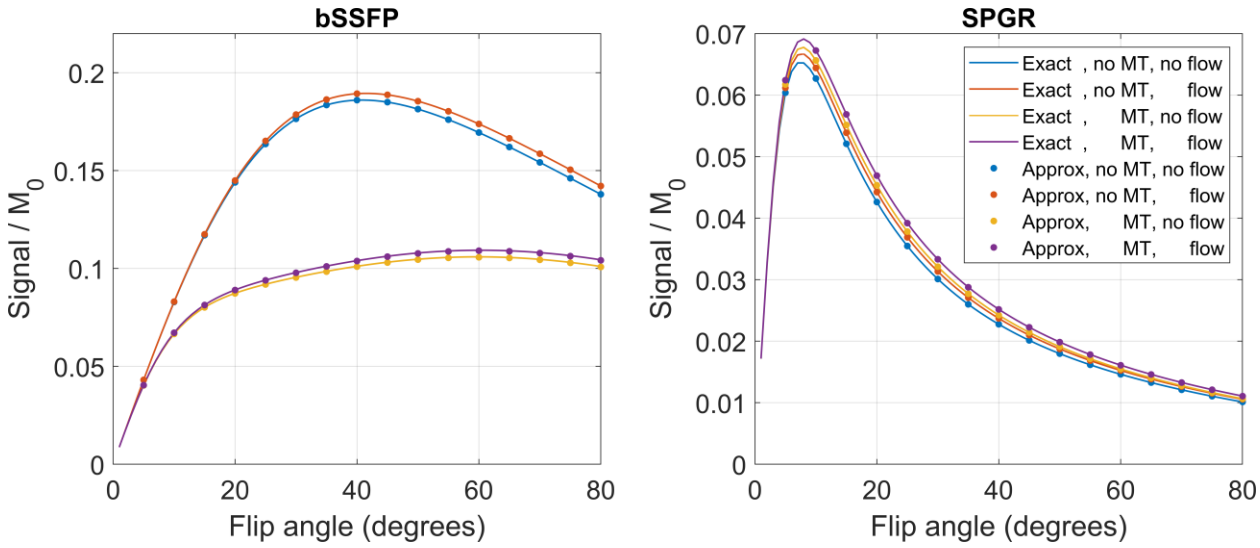

Supporting Information Figure S2. Simulations of steady-state (left) bSSFP and (right) SPGR signals for white matter at 1.5T obtained (blue) without MT and flow effects, (red) without MT and with flow effects, (orange) with MT and without flow effects, and (purple) with both MT and flow effects. Lines and dots indicate steady-state signals calculated without (Exact) and with (Approx.) the second approximation, respectively.

Supporting Information Table S1. Simulation parameters for Figure 3.

Type	Symbol	Parameter	Sweep: Range (min:step:max) Fixed: Value
Sweep	T_D	PASL transit delay	500:1:1500 (msec)
		PCASL transit delay	500:1:1500 (msec)
	T_W	PASL bolus duration	500:10:1000 (msec)
		PCASL bolus duration	1500:10:2000 (msec)
Fixed	F	Blood flow (low/high)	0.3/0.6 (mL/g/min)
	T_1	Spin-lattice relaxation of tissue	1200 (msec)
	T_2	Spin-spin relaxation of tissue	∞ (msec)
	Δf	Off-resonance	0 (Hz)
	T_{1b}	Spin-lattice relaxation of blood	1650 (msec)
	λ	Tissue/blood partition coefficient of water	0.9